

**Size and structure effect on optical transitions of iron oxide nanocrystals**

Y. P. He, Y. M. Miao, C. R. Li, S. Q. Wang, L. Cao, S. S. Xie, G. Z. Yang, and B. S. Zou\*  
*Nanoscale Physics and Device Laboratory, Institute of Physics, Chinese Academy of Sciences, Beijing 100080, China*

C. Burda

*Center for Chemical Dynamics and Nanomaterials Research, Department of Chemistry, Case Western Reserve University, Cleveland, OH 44106*

(Received 11 February 2004; revised manuscript received 23 November 2004; published 16 March 2005)

The heterogeneity of electronic states of transition metal oxides produces a variety of properties, which may be discerned by the measurements of their nanocrystals. The structure and optical spectra of chemically synthesized pure  $\text{Fe}_3\text{O}_4$ ,  $\gamma\text{-Fe}_2\text{O}_3$ , and  $\alpha\text{-Fe}_2\text{O}_3$  nanocrystals of different sizes have been investigated. Three types of electronic transitions: ligand to metal charge-transfer transitions, strong magnetic coupled  $\text{Fe}^{3+}$  ligand field transitions, and pair excitations, occur distinctly in the optical spectra of  $\gamma\text{-Fe}_2\text{O}_3$  and  $\alpha\text{-Fe}_2\text{O}_3$  nanocrystals except  $\text{Fe}_3\text{O}_4$ . The quantum size effect (for itinerant carriers) and finite size effect (for local magnetic moments) were observed in our nanocrystals, although their bulks are strong electron correlation systems. The localized to delocalized transformation of electrons occurs with time delay in the femtosecond transient absorption spectra of  $\alpha\text{-Fe}_2\text{O}_3$  nanocrystal sol, which indicates that heteroresponse times for different transitions agree well with the size-dependent indication of the steady-state absorption bands of these iron oxides nanocrystals. These results are helpful in understanding the relationship among  $d$ - $d$  transition, magnetic pairing, and charge-transfer in transition metal oxides.

DOI: 10.1103/PhysRevB.71.125411

PACS number(s): 78.40.Fy, 78.47.+p, 61.46.+w, 73.63.Bd

**I. INTRODUCTION**

Transition metal oxides (TMOs) are very important materials and belong to the system with strong electron-electron correlation and electron-phonon coupling, which lead to many complex phenomena<sup>1</sup> such as colossal magnetoresistance (CMR) in manganite, superconductivity in cuprate or water-intercalated sodium-cobalt oxide, magnetism in ferro or ferrite and ferroelectricity in titanate or niobate or tantalate. Moreover, these different physical properties may even show up in the same materials (like ferrite) and all of them exhibit size effects. The size effects reflect different critical physical lengths and behaviors for the varied elementary excitations and the interactions between these elementary excitations. However, up to now, there are some complicated or controversial theoretical and experimental descriptions on these properties and/or materials, for example, the relations between itinerant carriers and local  $d$ - $d$  transitions, the relations of collective excitation and single particle excitation and their respective response times. Moreover these relations and responding times are especially important for the varied electronic properties.

In the present work, we try to understand one typical system by using optical spectroscopic techniques. Iron oxides ( $\text{Fe}_3\text{O}_4$ ,  $\gamma\text{-Fe}_2\text{O}_3$ , and  $\alpha\text{-Fe}_2\text{O}_3$ ) belong to the representative TMO compounds with magnetism and semiconductor properties. Their magnetic performances have attracted much attention, but few on their itinerant electrons. The latter may be important in understanding their optical and electric properties including CMR under high frequency electric field. Although some steady-state spectroscopic results have been reported in some earlier literatures,<sup>2-5</sup> no systematic study on different iron oxide nanocrystals with different sizes was carried out. Nanometer-sized particles may serve a system for

investigating homogenous state discriminations, which may help the understanding of the electronic structure and properties of TMOs.

Nanometer-sized particles show a variety of properties as compared with the bulk system due to quantum size effect, finite size effect, and specific surface-area effect, which also show strong structure dependence. Many investigators have studied the structural transformation of various nanocrystals under pressure<sup>6-8</sup> and temperature.<sup>9</sup> The crystal structure even could transform by varying the synthesis route. Precipitation of pure  $\text{Fe}^{3+}$  ions by base typically produces an amorphous hydrated oxyhydroxide that can be easily converted to the corundum structure  $\alpha\text{-Fe}_2\text{O}_3$  with all  $\text{Fe}^{3+}$  having octahedral coordination.<sup>10</sup> By introducing  $\text{Fe}^{2+}$  cations having a stronger preference for octahedral site than  $\text{Fe}^{3+}$  cations, which causes some of the  $\text{Fe}^{3+}$  ions to occupy tetrahedral sites, the spinel structure  $\gamma\text{-Fe}_2\text{O}_3$  is favored during crystallization and oxidation process.<sup>11</sup> For the nanocrystals containing  $\text{Fe}^{3+}$  ions, the variation of crystal structure leads to the change of magnetic coupling strength and thus electronic transitions, which, in turn, can be reflected in their optical spectra. These indicate the intimate correlation of structural, electronic, optical, and magnetic properties.

In this paper, the optical spectral characteristics of the chemically synthesized various  $\text{Fe}_3\text{O}_4$ ,  $\gamma\text{-Fe}_2\text{O}_3$ , and  $\alpha\text{-Fe}_2\text{O}_3$  pure nanocrystals with different sizes have been investigated in detail. Their compositions and structures are verified with energy dispersive x-ray (EDX), x-ray photoelectron spectroscopy (XPS), x-ray powder diffraction (XRD), superconducting quantum interference device (SQUID) and UV-visible absorption measurements according to their specific characteristics indicated in literature. The different optical responses in the different energy and time scales, from local  $d$ - $d$  transitions to delocalized pair excita-

tions and charge-transfer transitions, are first observed by the femtosecond time-resolved absorption spectra, which are in accordance with the information indicated by the steady-state spectra. The steady-state spectra of the  $\gamma$ -Fe<sub>2</sub>O<sub>3</sub> and  $\alpha$ -Fe<sub>2</sub>O<sub>3</sub> show not only similarities but also discrepancies in the visible range. From the crystal size, structure, and electronic transition, the spectral discrepancies were analyzed.

## II. EXPERIMENT

### A. Synthesis

All the chemicals were of reagent grade and used without further purification. Ferric chloride hexahydrate (FeCl<sub>3</sub>·6H<sub>2</sub>O > 99%), ferrous sulfate heptahydrate (FeSO<sub>4</sub>·7H<sub>2</sub>O > 99%), sodium hydroxide (NaOH > 96%), potassium hydroxide (KOH > 96%), and potassium nitrate (KNO<sub>3</sub> > 99%) were obtained from Chemical Reagent Company in Beijing.

The magnetite (Fe<sub>3</sub>O<sub>4</sub>) nanocrystals with different sizes have been prepared by two kinds of synthesis routes and named according to their mean crystal size (in nanometers): samples M-7, M-40, and M-56. The sample M-7 was prepared by adding 100 ml of 1.5 M NaOH to 300 ml of an aqueous solution (0.1 M FeCl<sub>3</sub> and 0.05 M FeSO<sub>4</sub>) under constant stirring at room temperature. The samples M-40 and M-56 were obtained by the Matijevic's method,<sup>12</sup> that is, by heating at 90 °C a solution mixture of 0.2 M KOH and 0.2 or 0.105 M FeSO<sub>4</sub> for up to 4 h, in the presence of 0.2 M KNO<sub>3</sub>. The doubly distilled water was deoxygenated by bubbling N<sub>2</sub> gas for 1 h prior to use and all the main synthesis steps were carried out by passing N<sub>2</sub> gas through the solution media to avoid possible oxygen contamination during the operations. The formed black precipitate was separated by centrifugation and washed with the deoxygenated distilled water several times, then dried in the vacuum drying oven at 50 °C for 12 h.

The maghemite ( $\gamma$ -Fe<sub>2</sub>O<sub>3</sub>) nanocrystals with various shades of brown were obtained by oxidizing the corresponding Fe<sub>3</sub>O<sub>4</sub> (M-7, M-40, and M-56) nanocrystals in the electric muffle furnace at 180 °C for 8 h, 180 °C for 24 h, and 250 °C for 48 h, and denoted  $\gamma$ -10 (reddish brown),  $\gamma$ -47 (light brown), and  $\gamma$ -65 (pink brown), respectively.

The nonmagnetic hematite ( $\alpha$ -Fe<sub>2</sub>O<sub>3</sub>) nanocrystals with various shades of brown were prepared by a two-step method. First, adding 100 ml of 3 M NaOH to 400 ml of 0.2 M FeCl<sub>3</sub> aqueous solution under magnetic stirring at room temperature, the precipitate was instantly formed and separated by centrifugation and washed with water several times and dried in air. Then, the obtained nanocrystals were sintered in the electric muffle furnace at 300 °C for 2 h, 500 °C for 3 h, and 800 °C for 8 h, and denoted  $\alpha$ -12 (dark brown),  $\alpha$ -23 (reddish brown), and  $\alpha$ -48 (pink brown), respectively.

### B. Characterization

The structural properties of all the obtained nanocrystals were analyzed by XRD with a Bruker M18XHF diffractometer using the monochromatized x-ray beam from the Cu

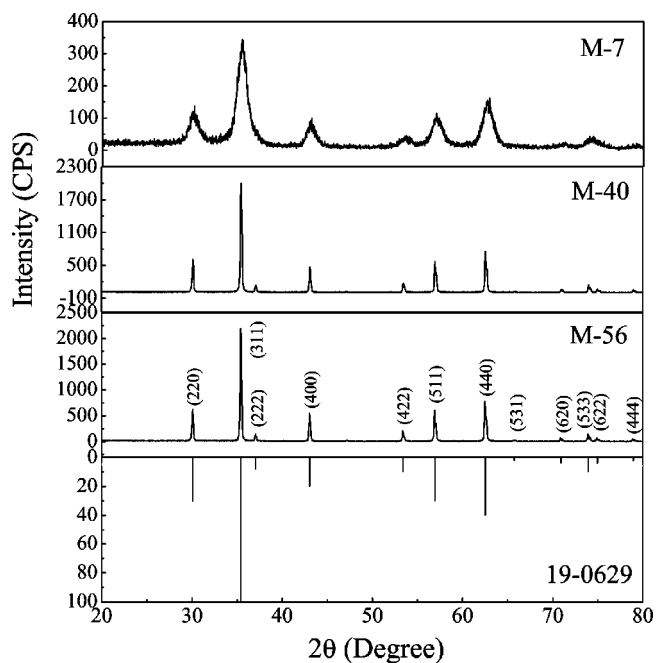


FIG. 1. X-ray diffraction patterns of the Fe<sub>3</sub>O<sub>4</sub> nanocrystals.

$K_{\alpha}$  radiation. The scanning voltage is 50 kV and the scanning current is 200 mA. The average size of the crystals ( $\bar{D}$  in nanometers) was estimated at first using Scherrer's formula<sup>13</sup> from the strongest peak in their x-ray diffraction patterns. Their transmission electron microscopy (TEM) images were obtained by using Philips CM12 microscope. The nanocrystals were coated with a layer of dodecyl benzene sulfonic acid sodium (DBS) in order to suppress the particle aggregation and then ultrasonically dispersed in an ethanol solution. A drop of such nanocrystal solution was cast on an amorphous carbon-coated copper grid and dried at room temperature for TEM observation.

The optical reflectance and absorption spectra in the range of 250–900 nm of the prepared nanocrystals were measured using a TU-1901 UV-visible spectrophotometer with an integrating sphere. The spectra were referenced against the compressed BaSO<sub>4</sub> powder.

The femtosecond (fs) absorption spectra of the  $\alpha$ -Fe<sub>2</sub>O<sub>3</sub> nanocrystals with the delay time were obtained with a pump-probe technique as described elsewhere<sup>14</sup> in detail.

In our experiment, a lot of samples were synthesized and characterized to confirm the result reproducibility, the crystal size, and structure effect on the optical transitions of iron oxide nanocrystals. The reproducibility is good according to the characterization results of XRD, EDX, XPS, SQUID, and optical absorption. The typical samples were selected to discuss in this paper. In addition, all these nanocrystals underwent a size selection using acetone solution to narrow their size distribution for further characterization.

## III. RESULTS AND DISCUSSION

### A. Crystal structure

Figures 1–3 show the x-ray diffraction patterns of the pre-

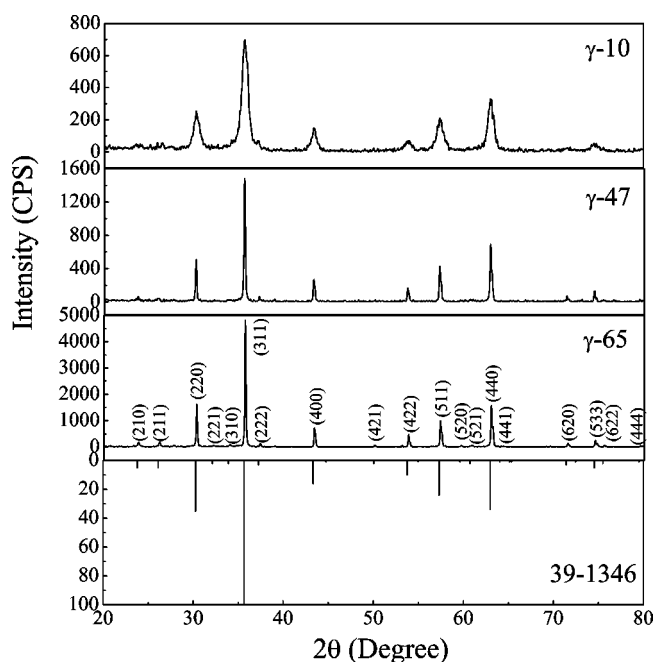


FIG. 2. X-ray diffraction patterns of the  $\gamma\text{-Fe}_2\text{O}_3$  nanocrystals.

pared  $\text{Fe}_3\text{O}_4$ ,  $\gamma\text{-Fe}_2\text{O}_3$ , and  $\alpha\text{-Fe}_2\text{O}_3$  nanocrystals accompanying with their standard ones, respectively. From these patterns, it is clear that all of the synthesized nanocrystals have a single phase and the crystal structures of the  $\text{Fe}_3\text{O}_4$ ,  $\gamma\text{-Fe}_2\text{O}_3$ , and  $\alpha\text{-Fe}_2\text{O}_3$  nanocrystals are separately in correspondence with those of Nos. 19-0629, 39-1346, and 33-0664 in Powder Diffraction File (PDF) collected by the Joint Committee on Powder Diffraction Standards (JCPDS). Their structure parameters are presented in Table I.

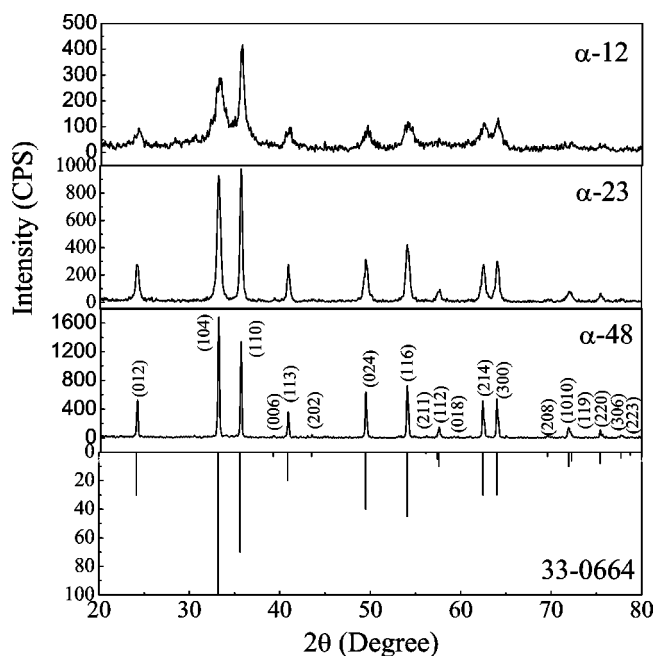


FIG. 3. X-ray diffraction patterns of the  $\alpha\text{-Fe}_2\text{O}_3$  nanocrystals.

TABLE I. Structure parameters for the obtained  $\text{Fe}_3\text{O}_4$ ,  $\gamma\text{-Fe}_2\text{O}_3$ , and  $\alpha\text{-Fe}_2\text{O}_3$  nanocrystals.

Sample	Structure type	$\bar{D}$ (nm)	Lattice parameter (nm)	
$\text{Fe}_3\text{O}_4$ (magnetite)	M-7	Cubic	7	
	M-40	( $Fd\bar{3}m$ )	40	$a \approx 0.839$
	M-56	Spinel	56	
$\gamma\text{-Fe}_2\text{O}_3$ (maghemite)	$\gamma$ -10	Cubic	10	
	$\gamma$ -47	( $P4_132$ )	47	$a \approx 0.835$
	$\gamma$ -65	Defect spinel	65	
$\alpha\text{-Fe}_2\text{O}_3$ (hematite)	$\alpha$ -12	Hexagonal	12	
	$\alpha$ -23	( $R\bar{3}C$ )	23	$a \approx 0.504$
	$\alpha$ -48	Corundum	48	$c \approx 1.375$

The representative TEM images of  $\gamma\text{-Fe}_2\text{O}_3$  nanocrystals are given in Fig. 4, from which the nanocrystals are all approximately spherical and the mean particle diameters of the  $\gamma$ -10 and  $\gamma$ -65 are  $\sim 10$  and  $\sim 60$  nm, respectively. The values match the 10 and 65 nm obtained by calculating the XRD data quite well. Moreover, the smaller the nanocrystal, the better the consistency of the sizes by both techniques is. As a result, the particle sizes calculated according to the XRD data can be adopted to analyze the size-dependent optical properties in the following sections.

## B. Theory of $\text{Fe}^{3+}$ spectra

It is well established<sup>2</sup> that three types of electronic transitions occur in the optical absorption spectra of  $\text{Fe}^{3+}$  substances—that is, the  $\text{Fe}^{3+}$  ligand field transitions or the  $d-d$  transitions, the ligand to metal charge-transfer transitions, and the pair excitations resulting from the simultaneous excitation of two neighboring  $\text{Fe}^{3+}$  cations that are magnetically coupled. The latter two concern the oxygen skeleton and may contribute to delocalized electrons in bulk.

### 1. $\text{Fe}^{3+}$ ligand field transitions or $\text{Fe}^{3+}$ $d-d$ transitions

In octahedral coordination, the Fe  $3d$  atomic orbitals are split into two sets of orbitals labeled as  $t_{2g}$  and  $e_g$ . The  $t_{2g}$  and  $e_g$  orbitals energy separation is the  $10Dq$  ligand field parameter or crystal field splitting. The  $t_{2g}$  and  $e_g$  orbitals are each split, in turn, by the exchange energy. The latter is related to the stabilization of electrons with majority spin ( $\alpha$  spin). The exchange splitting results in two sets of  $t_{2g}$  and  $e_g$  orbitals, one for the majority spin (spin-up or  $\alpha$  spin) and the other for the minority spin (spin-down or  $\beta$  spin) electrons. The ligand field transitions are between the states which arise from the different possible electronic configurations of the  $t_{2g}$  and  $e_g$  orbitals. The energies of the  $\text{Fe}^{3+}$  ligand field states as a function of  $10Dq$  are shown schematically in the well-known Tanabe-Sugano diagram in Fig. 5.

The ground  ${}^6A_1({}^6S)$  state in Fig. 5 arises from the ground state  $(t_{2g}^\alpha)^3(e_g^\alpha)^2$  configuration of high-spin  $\text{Fe}^{3+}$ . The first possible excited state configuration is  $(t_{2g}^\alpha)^3(e_g^\alpha)^1(t_{2g}^\beta)^1$ . The

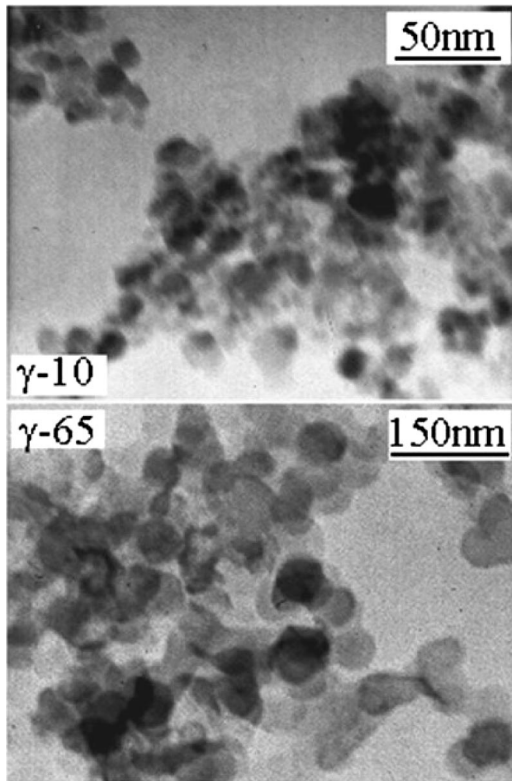


FIG. 4. TEM images of the representative  $\gamma\text{-Fe}_2\text{O}_3$  nanocrystals.

configuration gives the  ${}^4T_1({}^4G)$  and  ${}^4T_2({}^4G)$  states of Fig. 5. The remaining states in Fig. 5 result from the “spin-flip” configurations  $(t_{2g}^\alpha)^2(t_{2g}^\beta)^1(e_g^\alpha)^2$  and  $(t_{2g}^\alpha)^3(e_g^\alpha)^1(e_g^\beta)^1$ .

All of the transitions from the ground  ${}^6A_1({}^6S)$  state to the excited ligand field states are, in principle, both spin and laporte (or parity) forbidden. However, in practice these transitions may occur with a definite transition probability and be the origin of strong color of iron oxides. These transitions become allowed or assisted through the magnetic coupling of electronic spins of next-nearest neighbor  $\text{Fe}^{3+}$  cations in the crystal structure.<sup>15–18</sup> If two  $\text{Fe}^{3+}$  cations are strongly coupled, one must consider the spectroscopic selection rules for the  $\text{Fe}^{3+}\text{-Fe}^{3+}$  pairs but not those individual  $\text{Fe}^{3+}$  ions, at the moment the covalence between Fe and O also plays an important role. A qualitative understanding of the states associated with a  $\text{Fe}^{3+}\text{-Fe}^{3+}$  pair can be obtained by assuming that the coupling between the two  $\text{Fe}^{3+}$  centers is via the Heisenberg Hamiltonian

$$H = JS_a \cdot S_b. \quad (1)$$

Here,  $S_a$  and  $S_b$  are the electronic spins of the two  $\text{Fe}^{3+}$  cations and  $J$  is the Heisenberg exchange integral. Application of this Hamiltonian as a perturbation to the ligand field states of the uncoupled  $\text{Fe}^{3+}$  cations yields a set of states for the pair with energies given by

$$E = (J/2)[S(S+1) - S_a(S_a+1) - S_b(S_b+1)], \quad (2)$$

where  $S$  is the net spin of the pair with values  $|S_a+S_b|, |S_a+S_b-1|, \dots, |S_a-S_b|$ . If both  $\text{Fe}^{3+}$  cations are in their

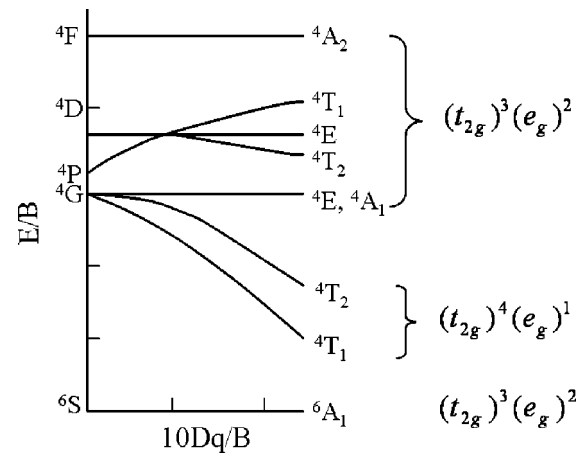


FIG. 5. Tanabe-Sugano diagram for high-spin  $\text{Fe}^{3+}$  in either octahedral or tetrahedral coordination.

ground  ${}^6A_1$  states,  $S_a=S_b=5/2$ ; the resulting pair-states derived by coupling the two  $\text{Fe}^{3+}$  cations will have  $S=0, 1, 2, 3, 4$ , and  $5$ . Now, if one of the  $\text{Fe}^{3+}$  cations in the pair is excited to a quartet ligand field state,  $S_a=3/2$  and  $S_b=5/2$ ; the two  $\text{Fe}^{3+}$  cations would therefore couple to give a set of pair states with  $S=1, 2, 3$ , and  $4$ . Transition from  $S=1, 2, 3$ , and  $4$  states in the  $\text{Fe}^{3+}({}^6A_1)\text{-Fe}^{3+}({}^6A_1)$  pair-state manifold to the states in the excited-single-ion pair-state manifold can, therefore, occur with  $\Delta S=0$  and be spin allowed. The relative energies of the states in the ground and excited-single-ion pair-state manifolds are shown in Fig. 6.

In iron oxides, some  $\text{O}^{2-}$  ions lie between the magnetically coupled two neighboring  $\text{Fe}^{3+}$  ions, meaning the overlapping or hybridization between  $\text{Fe } 3d$  and  $\text{O } 2p$  orbitals, and thus relax the Laporte-forbidden transition to some extent. Therefore, both the spin and Laporte selection rules for the  $\text{Fe}^{3+}$  ligand field transitions can be relaxed by the magnetic coupling of adjacent  $\text{Fe}^{3+}$  cations and covalent bonding with oxygen. Moreover, this covalent bonding may be enhanced by decreasing size and surface modification.<sup>19</sup>

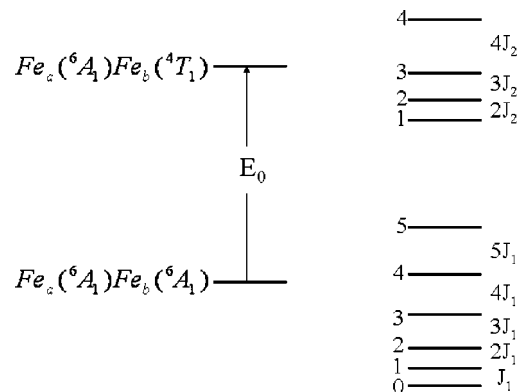


FIG. 6. States of a  $\text{Fe}^{3+}\text{-Fe}^{3+}$  pair assuming that the  $\text{Fe}^{3+}$  cations are coupled via the Heisenberg Hamiltonian.  $E_0$  is the energy difference between the ground  ${}^6A_1$  state and an arbitrary quartet state of an isolated, uncoupled  $\text{Fe}^{3+}$  cation. The numbers next to each level indicate the spin quantum number ( $S$ ) of the pair state.

2. Pair excitations or double exciton processes

An additional phenomenon resulting from the magnetic coupling of adjacent Fe<sup>3+</sup> cations is the presence of absorption features corresponding to the simultaneous excitation of two Fe<sup>3+</sup> centers.<sup>18</sup> These features occur at energies given approximately by the sum of two single-ion Fe<sup>3+</sup> ligand field transitions and are often referred to as “double exciton processes.” These transitions are also spin allowed: if both Fe<sup>3+</sup> cations are excited to a quartet ligand field state so that  $S_a = S_b = 3/2$ , the pair states resulting from coupling the two Fe<sup>3+</sup> cations will have  $S$  values of 0, 1, 2, and 3. Transitions to these pair states can therefore occur from the  $S=0, 1, 2$ , and 3 states in the Fe<sup>3+</sup>(<sup>6</sup>A<sub>1</sub>)-Fe<sup>3+</sup>(<sup>6</sup>A<sub>1</sub>) ground state manifold.

3. Ligand to metal charge-transfer transitions

According to molecular orbital theory, the transitions at energy higher than most of the ligand field transitions are the ligand to metal charge-transfer transitions (LMCT). Bands above 400 nm in energy were assigned to LMCT transitions.<sup>2</sup> However, in real bulk ferric oxide, this charge-transfer band tail may extend to longer wavelength region with the assistance of magnetic coupling. The characteristics can also be found evidence from the result of ferric oxide nanoclusters.<sup>20</sup>

4. Band edge of ferric oxide and narrow  $d$  bands

The band edge of inorganic solid is located at the low energy end of continuum band above the valence band. It is difficult to determine the band edge for TMO because there are a lot of narrow  $d$ - $d$  bands in the gap, and even some extend to infrared region with a definite probability. It is well accepted that the band edge of Fe<sub>2</sub>O<sub>3</sub> is located in the range of 580–620 nm.<sup>2</sup> Clearly the transitions in this energy region include the  $d$ - $d$  transition, pair excitation, and less charge transfer, and the former two transitions mainly come from the narrow  $d$  bands, so the optical properties of Fe<sub>2</sub>O<sub>3</sub> band edge cannot be accounted for intrinsic semiconductor. The short photoexcited electron lifetime of Fe<sub>2</sub>O<sub>3</sub> nanoclusters provides evidence for the fast relaxation of neighboring  $d$  levels.<sup>20</sup>

C. Experimental study on optical spectral characteristics of iron oxides

The optical absorption and reflectance spectra in the range of 250–900 nm of as-synthesized  $\gamma$ -Fe<sub>2</sub>O<sub>3</sub> and  $\alpha$ -Fe<sub>2</sub>O<sub>3</sub> nanocrystals are shown in Figs. 7 and 8. Figures 7(a) and 8(a) are the absorption ones and Figs. 7(b) and 8(b) are the reflectance ones.

From Figs. 7(a) and 8(a), it is clear that four unambiguous absorption regions appear in the absorption spectra of the  $\gamma$ -Fe<sub>2</sub>O<sub>3</sub> and  $\alpha$ -Fe<sub>2</sub>O<sub>3</sub> nanocrystals. According to the Refs. 2 and 3, region 1 (250–400 nm) mainly results from the ligand to metal charge-transfer transitions and partly from the contributions of the Fe<sup>3+</sup> ligand field transitions <sup>6</sup>A<sub>1</sub> → <sup>4</sup>T<sub>1</sub>(<sup>4</sup>P) at 290–310 nm, <sup>6</sup>A<sub>1</sub> → <sup>4</sup>E(<sup>4</sup>D) and <sup>6</sup>A<sub>1</sub> → <sup>4</sup>T<sub>2</sub>(<sup>4</sup>D) at 360–380 nm. Region 2 (400–600 nm) is considered to be

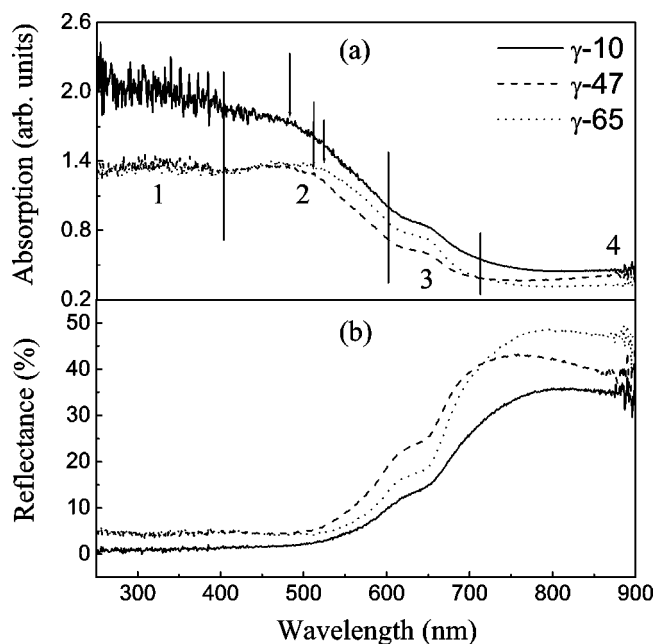


FIG. 7. (a) Absorption and (b) reflectance spectra of the  $\gamma$ -Fe<sub>2</sub>O<sub>3</sub> nanocrystals of different sizes.

the result of the pair excitation processes <sup>6</sup>A<sub>1</sub>+<sup>6</sup>A<sub>1</sub> → <sup>4</sup>T<sub>1</sub>(<sup>4</sup>G)+<sup>4</sup>T<sub>1</sub>(<sup>4</sup>G) at 485–550 nm, possibly overlapped the contributions of <sup>6</sup>A<sub>1</sub> → <sup>4</sup>E, <sup>4</sup>A<sub>1</sub>(<sup>4</sup>G) ligand field transitions at 430 nm and the charge-transfer band tail. Region 3 (600–750 nm) is assigned to the <sup>6</sup>A<sub>1</sub> → <sup>4</sup>T<sub>2</sub>(<sup>4</sup>G) transition at about 640 nm and region 4 (750–900 nm) is the <sup>6</sup>A<sub>1</sub> → <sup>4</sup>T<sub>1</sub>(<sup>4</sup>G) transition at about 900 nm. Moreover, the absorption intensity in regions 1 and 2 is far larger than that in regions 3 and 4, which indicates that the absorption from the

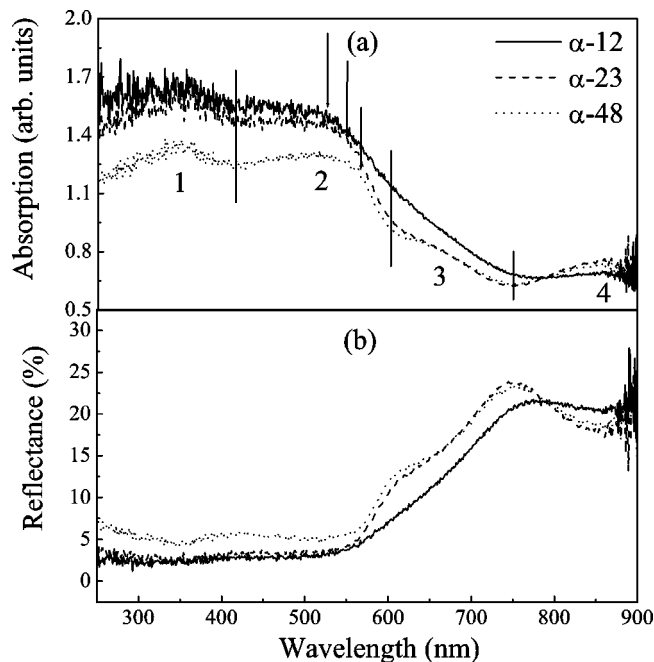


FIG. 8. (a) Absorption and (b) reflectance spectra of the  $\alpha$ -Fe<sub>2</sub>O<sub>3</sub> nanocrystals of different sizes.

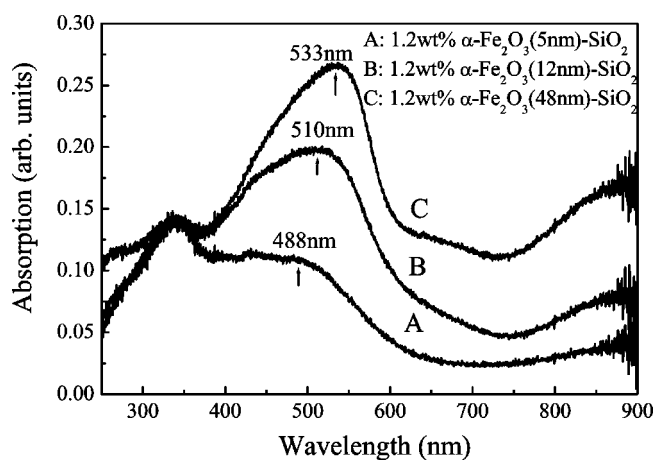


FIG. 9. Absorption spectra of the 1.2 wt %  $\alpha$ -Fe<sub>2</sub>O<sub>3</sub> nanocrystals of different sizes in SiO<sub>2</sub> powders.

charge-transfer transitions or the pair excitations is far stronger than that from the ligand field transitions due to the selection rules.

The experimental results on the different samples have been obtained under the same conditions (concentration, light, sample thickness), so they can be used for comparison. By carefully analyzing these spectra, one can see that the crystal size has little effect on the absorption bands in regions 1, 3, and 4; while the band in region 2 blueshifts visibly with reducing size: for the  $\gamma$ -Fe<sub>2</sub>O<sub>3</sub> nanocrystals, the absorption band shifts in wavelength from about 475 nm for sample  $\gamma$ -10, 504 nm for  $\gamma$ -47 to 510 nm for  $\gamma$ -65; for  $\alpha$ -Fe<sub>2</sub>O<sub>3</sub> nanocrystals, the absorption band shifts from about 490 nm for sample  $\alpha$ -12, 510 nm for  $\alpha$ -23 to 517 nm for  $\alpha$ -48. For further verification, we compared the absorption spectra of  $\alpha$ -Fe<sub>2</sub>O<sub>3</sub> nanocrystals dispersed in SiO<sub>2</sub> powders in Fig. 9, the size related absorption band shift (spectral weight) shows up clearly except the local transitions. This experiment coincides with the previous measurement of quantum confinement. These results indicate that the electrons in this energy range are delocalized, for which the evidence can be also found from the previous work of Zou *et al.*<sup>19,21</sup> and the recent observed photovoltaic responses. Hence, the quantum confinement takes effect in such TMO nanocrystals.

From Fig. 9, we also observe another phenomenon, the relative intensities of different regions change with varying size. Why does this happen? It is due to the pair excitation is enhanced for larger particles together with the charge-transfer band redshift. This variation is in agreement with our assignment of transitions in Fe<sub>2</sub>O<sub>3</sub> nanocrystals.

The optical absorption spectrum of solid obtained by a UV-visible spectrophotometer is the integrated optical-matter interaction responses of all irradiated nanocrystals in all time scales. It is supposed that the dynamic processes of the above-mentioned transitions with varied nature be different, however, they cannot be distinguished via the steady-state spectra by now. Most of the theoretical models also treat the electronic states in a phenomenological way. These blocked the understanding of the inner nature of these electronic states, which may be clearly revealed by the fs time-resolved

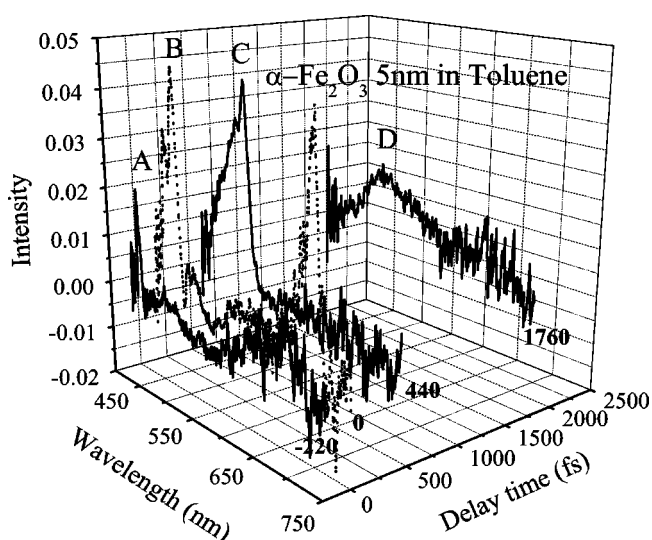


FIG. 10. Femtosecond time-resolved absorption spectra of the 5 nm  $\alpha$ -Fe<sub>2</sub>O<sub>3</sub> organosol in toluene at the representative delay times.

spectra. Using nanocrystals can avoid the light scattering for further analysis. Figure 10 is the fs absorption spectra of 5 nm  $\alpha$ -Fe<sub>2</sub>O<sub>3</sub> organosol in toluene at varied delay times under 400 nm pump, where curve A denotes the one measured at 220 fs ahead of the pump light excitation and curves B, C, and D denote the ones at 0, 440, and 1760 fs after excitation, respectively. The transient absorption signal is rather weak, although the surfactant capping can enhance the absorption coefficient. Prior to light excitation, the weak sharp peaks in curve A are the linear absorption, all from the local  $d$ - $d$  transitions of the single Fe<sup>3+</sup> ion in  $\alpha$ -Fe<sub>2</sub>O<sub>3</sub> nanocrystals. Once the sample is excited by pump light, the spectra represent the nonlinear absorption. In the range of 0–440 fs, its positive absorption (B curve) comes from the local Fe<sup>3+</sup> ions due to the allowed two-photon transition. Two bands appear at 480 and 700 nm, respectively, with much larger oscillator strength than the linear absorption, but the latter (700 nm) shows a much shorter lifetime than 440 fs due to the local transition nature on one Fe ion. In the scale of 440 fs to longer times, the electronic wave function of excitation state in nanocrystals rapidly extends to multiatoms, and the charge transfer and magnetic coupling interactions occur between the Fe-O bonds and the neighboring Fe<sup>3+</sup> ions, and thus produce the enhanced broad absorption with a longer lifetime to nanosecond (ns) scale.<sup>14</sup> Figure 11 gives the transient absorption decay profiles of  $\alpha$ -Fe<sub>2</sub>O<sub>3</sub> nanocrystals probed at 500, 600, and 700 nm, and their dominant lifetimes are 195, 38, and 86 fs, respectively, although there exist some longer lifetime components. The lifetime scales reflect the nature of varied transitions at different wavelengths. These results seem a little different from that by Zhang *et al.*<sup>20</sup> For our sample, the lifetimes at varied wavelengths are shorter than theirs on one hand; on the other hand, our decay profiles are dependent of the probe wavelength—the lifetime in the range of 450–550 nm is long but those at 700 and 600 nm are short. The data did not change with surface modification for large nanocrystals

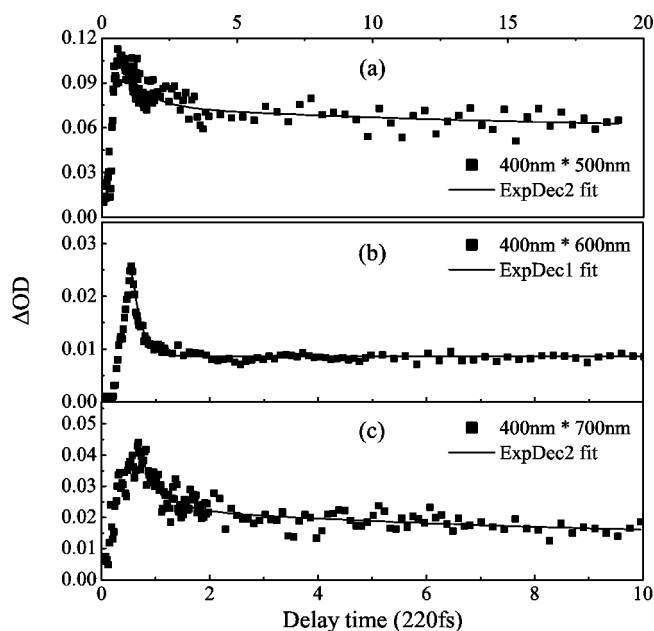


FIG. 11. Transient absorption decay profile probed at (a) 500, (b) 600, and (c) 700 nm for the 5 nm  $\alpha$ - $\text{Fe}_2\text{O}_3$  organosol.

(above 5 nm). That is to say, the data (by our two groups) at about 600–700 nm reflect the  $d$ - $d$  transition with a short lifetime, but the data in the range of 450–550 nm are different. Hence, the pair excitations, by contrast with the single  $\text{Fe}^{3+}$  ion absorption, increase the lifetime of 480 nm band and extend it up to 550 nm, as shown in the C and D curves. Those bands in the red region (600–750 nm) rapidly relax, but those in the region 450–550 nm gradually become broader and weaker with delay time in Fig. 10. Clearly this spectral broadening originates from the relaxation of the partial electrons in  $\text{Fe}^{3+}$  ions to the adjacent  $\text{O}^{2-}$  ions or neighboring Fe ions, and thus the electrons with this energy become delocalized and itinerant in the single nanocrystal. As a result, the different optical responses in the different energy and time scales, (1) from local  $d$ - $d$  transitions to delocalized pair excitations and charge transfer transitions (450–550 nm), (2)  $d$ - $d$  transitions (550–750 nm), can be clearly distinguished by the transient absorption spectra.

The transient absorption spectra indicate that only the band around 450–550 nm, from partially delocalized states, could show quantum confinement, which was reflected by the corresponding band in the steady-state spectra that extends continually to longer wavelength until 600 nm, similar to the band edge of bulk. The emission measurement of 5 nm  $\alpha$ - $\text{Fe}_2\text{O}_3$  shows the band edge emission<sup>22</sup> is in the range of 570–590 nm, although there exist weak emission below 600 nm in energy. From this result and the above fs measurement, we realize the spectral range around 600 nm should be a turning point (band edge). In addition, some  $d$ - $d$  transitions may exhibit a finite size effect due to the magnetic correlation if the direction of the electronic spins is satisfied. We cannot see the finite size effect of magnetism in the fs range because of the long-range magnetic correlations, which can be detected in the ns range.<sup>14</sup> All these dynamic results of different electronic states and the transformation between

them provide strong bases for the miscellaneous electronic and optical behaviors occurred in the iron oxide nanocrystals.

Then let us go back to the steady-state spectra. From Figs. 7(a) and 8(a), it also can be seen that the absorption coefficients as a whole increase with decreasing size, which comes from the specific size effect. The smaller the crystal, the bigger the specific transmission depth and thus the more the incident light absorbed by the nanocrystals is. However, for the  $\gamma$ - $\text{Fe}_2\text{O}_3$  nanocrystals, in the range of 450–710 nm, the absorption intensity of the sample  $\gamma$ -47 is on the contrary smaller than that of the  $\gamma$ -65, which is possibly relevant to the band edge redshift in the region 2 for the  $\gamma$ -65 relative to the  $\gamma$ -47. In region 4, the absorption coefficients of the samples  $\gamma$ -10 and  $\gamma$ -65 almost do not change, but that of the  $\gamma$ -47 increases gradually with wavelength, which means the absorption band at about 900 nm will appear in this sample. For the  $\alpha$ - $\text{Fe}_2\text{O}_3$  nanocrystals, a distinct absorption band at about 860 nm appears in all the three spectra. When the wavelength is longer than 800 nm, the absorptions of the samples  $\alpha$ -23 and  $\alpha$ -48 are, on the contrary, stronger than that of the  $\alpha$ -12.

The change of the absorption coefficient with the crystal size in region 4 is an abnormal phenomenon. This abnormal absorption can be more clearly shown in the reflectance spectra of Figs. 7(b) and 8(b), and probably originates from a so-called finite size effect—i.e., the specific physical parameter, the absorption coefficient, reaches its maximum at a certain critical size. For  $\gamma$ - $\text{Fe}_2\text{O}_3$ , the size may be ascribed to magnetic single domain. Its critical size at about 47 nm is close to 50 nm that is obtained from the magnetic measurement of isostructural  $\text{Fe}_3\text{O}_4$  nanocrystals,<sup>23</sup> in which the magnetic performance reduces when the crystal size becomes larger or smaller than the critical single-domain size. But for the  $\alpha$ - $\text{Fe}_2\text{O}_3$ , the critical size is only about 23 nm and may analogously come from the composite result of the intraparticle exchange interactions and magnetic anisotropy (cant magnetism).<sup>24</sup>

The absorption spectra of the  $\gamma$ - $\text{Fe}_2\text{O}_3$  and  $\alpha$ - $\text{Fe}_2\text{O}_3$  nanocrystals with the approximately same size are shown in Fig. 12. For comparison, the spectra of as synthesized  $\text{Fe}_3\text{O}_4$  samples with the smallest and the biggest size are also given. Light in the range of 250–900 nm can be strongly absorbed by  $\text{Fe}_3\text{O}_4$  nanocrystals, which makes it difficult to resolve the different transitions in the spectra, but the absorption coefficient versus the crystal size still resembles that of the other two iron oxides and the abnormal absorption variation with size also occurs in the long wavelength region.

By comparing the absorption spectra of the  $\gamma$ -47 and the  $\alpha$ -48, one can see that (1) for the absorption intensities at short wavelength region—mostly by the charge-transfer transition, the former is stronger than the latter. This accords with the conclusion that the charge-transfer contribution to  $\gamma$ - $\text{Fe}_2\text{O}_3$  is larger than that to  $\alpha$ - $\text{Fe}_2\text{O}_3$ ;<sup>3</sup> (2) The light absorbing ability of  $\alpha$ - $\text{Fe}_2\text{O}_3$  in long wavelength region is far stronger than that of  $\gamma$ - $\text{Fe}_2\text{O}_3$ ; (3) The band of  $\gamma$ - $\text{Fe}_2\text{O}_3$  in region 2 blueshifts relative to that of the  $\alpha$ - $\text{Fe}_2\text{O}_3$ ; (4) The band of  $\alpha$ - $\text{Fe}_2\text{O}_3$  in region 3 (600–750 nm) obviously broadens as compared with that of the  $\gamma$ - $\text{Fe}_2\text{O}_3$ .

We first discuss the difference in crystal structure between  $\alpha$ - $\text{Fe}_2\text{O}_3$  and  $\gamma$ - $\text{Fe}_2\text{O}_3$  in relation to their optical properties.

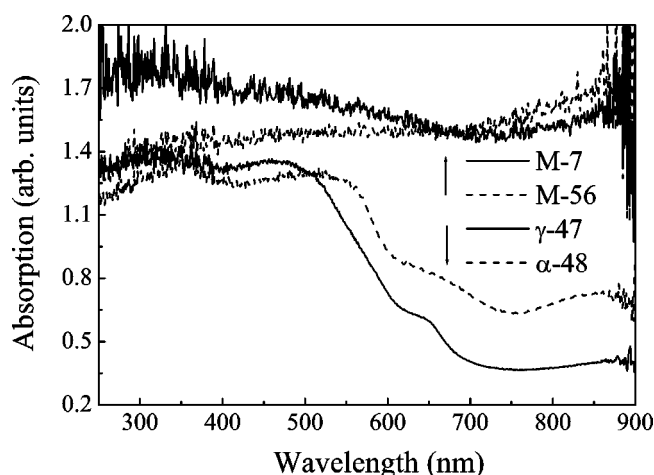


FIG. 12. Absorption spectra of the  $\text{Fe}_3\text{O}_4$ ,  $\gamma\text{-Fe}_2\text{O}_3$ , and  $\alpha\text{-Fe}_2\text{O}_3$  nanocrystals.

$\alpha\text{-Fe}_2\text{O}_3$  is a uniaxial hexagonal crystal (space group:  $R\bar{3}C$ ) with electronic anisotropy and has a corundum structure with distorted  $\text{FeO}_6$  octahedra. The octahedra is connected to the nearest neighboring ones via face-sharing bonds in addition to corner and edge-sharing ones.<sup>4</sup> While,  $\gamma\text{-Fe}_2\text{O}_3$  is a cubic crystal (space group:  $P4_132$ ) and has a cation-deficient spinel ( $\text{Fe}^{3+}$ ) [ $\square_{1/3}\text{Fe}^{3+}_{5/3}$ ] structure. Here, the parenthesis denotes A site and square bracket denotes B site. In a spinel, the cations in A and B sites have tetrahedral  $\text{FeO}_4$  and octahedral  $\text{FeO}_6$  coordination with oxygen, respectively, and in the former a central Fe atom is surrounded by the corner-sharing oxygens only and the latter contains both corner and edge-sharing oxygens (Fig. 13).

The face-sharing  $\text{FeO}_6$  octahedra in  $\alpha\text{-Fe}_2\text{O}_3$  results in a trigonal distortion of the  $\text{FeO}_6$  coordination polyhedra, which produces stronger antiferromagnetic coupling between the neighboring Fe ions than that in  $\gamma\text{-Fe}_2\text{O}_3$  (see Ref. 5) on one hand; on the other hand, the symmetry of  $\alpha\text{-Fe}_2\text{O}_3$  is lowered and then gives rise to more relaxed Laporte-forbidden transitions than in  $\gamma\text{-Fe}_2\text{O}_3$ . Moreover, there is no defect  $\text{FeO}_6$  octahedral sites in  $\alpha\text{-Fe}_2\text{O}_3$  as compared with one-sixth  $\text{FeO}_6$  defect sites in  $\gamma\text{-Fe}_2\text{O}_3$ . Just the above two reasons, espe-

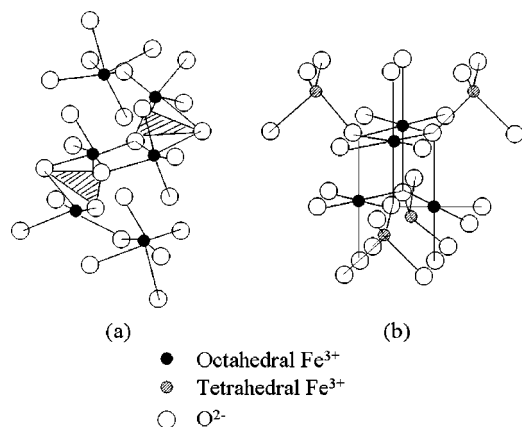


FIG. 13. Linkage mode of oxygen polyhedra in (a) Corundum type  $\alpha\text{-Fe}_2\text{O}_3$  and (b) Spinel type  $\gamma\text{-Fe}_2\text{O}_3$ .

cially the first one leads to a larger transition probability of the spin-allowed single-ion excitation and simultaneous double-ion excitation (often referred as pair excitations or double exciton processes) of two  $\text{Fe}^{3+}$  centers for  $\alpha\text{-Fe}_2\text{O}_3$  than  $\gamma\text{-Fe}_2\text{O}_3$ . In region 2, the double exciton processes [ ${}^6A_1 + {}^6A_1 \rightarrow {}^4T_1({}^4G) + {}^4T_1({}^4G)$  at 485–550 nm] prevail over the single exciton ones [ ${}^6A_1 + {}^6A_1 \rightarrow {}^4E, {}^4A_1({}^4G) + {}^6A_1$  “exciton + magnon” transition at 430 nm] and the charge-transfer band tail in the case of the face-sharing  $\alpha\text{-Fe}_2\text{O}_3$ , and quite the reverse in the case of  $\gamma\text{-Fe}_2\text{O}_3$ . Thus, that the absorption band of  $\gamma\text{-Fe}_2\text{O}_3$  in this region blueshifts relative to that of  $\alpha\text{-Fe}_2\text{O}_3$  can be easily understood.

In the long wavelength region, just the spin-allowed single-ion excitations and relaxed Laporte-forbidden transitions of the  $\text{Fe}^{3+}$  ligand field transitions with higher transition probability produce far stronger absorption for the  $\alpha\text{-Fe}_2\text{O}_3$  than the  $\gamma\text{-Fe}_2\text{O}_3$ . This agrees well with the reported third-order nonlinear optical susceptibility  $\chi^{(3)}$  values of  $5.8 \times 10^{-11}$  for  $\alpha\text{-Fe}_2\text{O}_3$  larger than  $2.1 \times 10^{-11}$  for  $\gamma\text{-Fe}_2\text{O}_3$  (see Ref. 3) because the nonlinear optical susceptibility to a large extent reflects the nonlinear optical absorption. The spin canting effect on the surface of the antiferromagnetic  $\alpha\text{-Fe}_2\text{O}_3$  nanocrystals induces the weak ferromagnetic interaction between interstitial  $\text{Fe}^{3+}$  ions,<sup>25,26</sup> which is expressed in energy diagram that the distribution of the energy difference  $\Delta E$  between the ground  ${}^6A_1$  state and the excited states  ${}^4T_2({}^4G)$  becomes wide, hence the band of the  $\alpha\text{-Fe}_2\text{O}_3$  in region 3 (600–750 nm) broadens as compared with that of the  $\gamma\text{-Fe}_2\text{O}_3$ .

The  $\text{Fe}_3\text{O}_4$  nanocrystals show strong and no structured absorption in the UV-visible range. The intervalence charge transfer (IVCT) is important, almost covering the whole spectral region,<sup>27</sup> although all above-mentioned transitions in  $\text{Fe}_2\text{O}_3$  exist in  $\text{Fe}_3\text{O}_4$ . The magneto-optical (MO) measurements can be used to distinguish the different transitions in  $\text{Fe}_3\text{O}_4$ .<sup>28,29</sup> Fontijn *et al.*<sup>28</sup> reported the 0.5–4.0 eV MO response and obtained the imaginary part of the off-diagonal element of the dielectric tensor of  $\text{Fe}_3\text{O}_4$ , which can be related to the magnetic absorption. Their profiles also can be separated into four regions: (1) 4–2.75 eV, IVCT + charge transfer between  $\text{Fe}^{3+}$  and O; (2) 2.75–2 eV, IVCT + pair excitations; (3) 2–1.3 eV, single  $d-d$  transition of  $\text{Fe}^{3+}$  + IVCT; (4) below 1.3 eV, single  $d-d$  transition of  $\text{Fe}^{2+}$  + IVCT. Such assignment agrees well with the defining of our experimental data. As to the size-dependent transition variation, Barnakov *et al.*<sup>29</sup> reported the spectral shift of Faraday rotation of different sized  $\text{Fe}_3\text{O}_4$  nanocrystals. Although their absorption spectra of  $\text{Fe}_3\text{O}_4$  polymer is similar to that of  $\gamma\text{-Fe}_2\text{O}_3$  (there may contain some  $\gamma\text{-Fe}_2\text{O}_3$ ), the size-dependent shifts of negative band center of Faraday rotation spectra were clearly observed from wavelength of 620 nm for 200 nm particles to 440 nm for 8 nm particles. The particle aggregation of 8 nm particles also produce similar shift of the delocalized band in this region.<sup>29</sup> This spectral range is related to region 2 in our assignment, magnetic pairing excitation plus some charge-transfer component, in our  $\text{Fe}_2\text{O}_3$  systems. This also proved the delocalization of magnetic excitons in this range.

In our work,  $\alpha\text{-Fe}_2\text{O}_3$  nanocrystals obtained by the oxidation of  $\text{Fe}_3\text{O}_4$  at high temperature are also investigated, and

the results show that the optical variation tendency is the same as that of the directly synthesized ones. This indicates that, for the iron oxide with the same structure, the optical transition is insensitive to the synthesis route and thus embodies their intrinsic feature in some sense.

#### IV. SUMMARY

The  $\text{Fe}_3\text{O}_4$ ,  $\gamma\text{-Fe}_2\text{O}_3$ , and  $\alpha\text{-Fe}_2\text{O}_3$  pure nanocrystals have been successfully synthesized by the chemical method. The optical spectra in the range of 250–900 nm were carefully investigated. There were not only some similarities but also discrepancies in the whole spectra of various iron oxide nanocrystals. Three types of electronic transitions can be distinguished in the  $\gamma\text{-Fe}_2\text{O}_3$  and  $\alpha\text{-Fe}_2\text{O}_3$  nanosystems.  $\text{Fe}_3\text{O}_4$  nanocrystals have strong absorption with no structure in the visible region, and thus it is difficult to resolve its different transitions, however, its magneto-optical responses can reflect the above-mentioned three transitions besides IVCT. The steady spectroscopic results can be well found indication from the fs absorption spectra and lifetime profiles of  $\alpha\text{-Fe}_2\text{O}_3$  nanocrystals. Although bulk iron oxides were conven-

tionally considered as a system with strong local electron correlation, quantum size effect as well as finite size effect took place in these as-prepared nanocrystals with varying size. That the magnetic coupling between the neighboring  $\text{Fe}^{3+}$  ions and the transfer of the partial electrons in  $\text{Fe}^{3+}$  ions to the adjacent  $\text{O}^{2-}$  ions shows that the electrons in iron oxides are delocalized, which causes a blueshift in the band of 400–600 nm with reducing size. In addition, the relative change of the absorption intensity in the range of 750–900 nm with the crystal size is in good agreement with the size-related magnetic response of iron oxide nanocrystals, i.e., so called finite size effect. The spectroscopic discrepancy between the same sized  $\gamma\text{-Fe}_2\text{O}_3$  and  $\alpha\text{-Fe}_2\text{O}_3$  was analyzed from their structure difference. These results are important to understand the electronic structure and magneto-optical properties of iron oxides.

#### ACKNOWLEDGMENTS

The authors would like to thank the National Natural Science Foundation of China under Grant No. 20173073 and the Hundred Talents Project of the Chinese Academy of Sciences for financial support.

\*Email address: zoubs@aphy.iphy.ac.cn

- <sup>1</sup>Y. Tokura and N. Nagaosa, *Science* **288**, 462 (2000); K. Takada, H. Sakurai, E. Takayama-Muromachi, F. Izumi, R. A. Dilanian, and T. Sasaki, *Nature (London)* **422**, 53 (2003).
- <sup>2</sup>D. M. Sherman and T. D. Waite, *Am. Mineral.* **70**, 1262 (1985).
- <sup>3</sup>T. Hashimoto, T. Yamada, and T. Yoko, *J. Appl. Phys.* **80**, 3184 (1996).
- <sup>4</sup>S. Nagel, *J. Phys. Chem. Solids* **46**, 905 (1985).
- <sup>5</sup>D. M. Sherman, *Phys. Chem. Miner.* **12**, 161 (1985).
- <sup>6</sup>S. H. Tolbert and A. P. Alivisatos, *Annu. Rev. Phys. Chem.* **46**, 595 (1995).
- <sup>7</sup>Z. Y. Wu, Z. X. Bao, L. Cao, C. X. Liu, Q. S. Li, S. S. Xie, and B. S. Zou, *J. Appl. Phys.* **93**, 9983 (2003).
- <sup>8</sup>N. Mōri, S. Todo, N. Takeshita, T. Mori, and Y. Akishige, *Physica B* **312–313**, 686 (2002).
- <sup>9</sup>P. Poddar, T. Fried, G. Markovich, A. Sharoni, D. Katz, T. Wizansky, and O. Millo, *Europhys. Lett.* **64**, 98 (2003).
- <sup>10</sup>U. Schwertmann and E. Murad, *Clays Clay Miner.* **31**, 227 (1983).
- <sup>11</sup>E. Tronc and J. P. Jolivet, in *Nanophase Materials*, edited by G. C. Hadjipanayis and R. W. Siegel (Kluwer, Dordrecht, 1994), p. 21.
- <sup>12</sup>T. Sugimoto and E. Matijevic, *J. Colloid Interface Sci.* **74**, 227 (1980).
- <sup>13</sup>R. Massart and V. Cabuil, *J. Phys. Chem.* **84**, 967 (1987).
- <sup>14</sup>L. M. Fu, Z. Y. Wu, X. C. Ai, J. P. Zhang, Y. X. Nie, S. S. Xie, G. Z. Yang, and B. S. Zou, *J. Chem. Phys.* **120**, 3406 (2004).
- <sup>15</sup>J. Ferguson, H. J. Guggenheim, and Y. Tanabe, *J. Phys. Soc. Jpn.* **21**, 347 (1966).
- <sup>16</sup>J. J. Krebs and W. G. Maisch, *Phys. Rev. B* **4**, 757 (1971).
- <sup>17</sup>L. L. Lohr, *Coord. Chem. Rev.* **8**, 241 (1972).
- <sup>18</sup>H. J. Schugar, G. R. Rossman, J. Thibeault, and H. B. Gray, *Chem. Phys. Lett.* **6**, 26 (1970).
- <sup>19</sup>B. S. Zou, J. Jin, and J. Xu, *Phys. Low-Dimens. Semicond. Struct.* **1/2**, 173 (1996).
- <sup>20</sup>N. J. Cherepy, D. B. Liston, J. A. Lovejoy, H. Deng, and J. Z. Zhang, *J. Phys. Chem. B* **102**, 770 (1998).
- <sup>21</sup>B. S. Zou, W. Huang, M. Y. Han, S. F. Y. Li, X. C. Wu, Y. Zhang, J. S. Zhang, P. F. Wu, and R. Y. Wang, *J. Phys. Chem. Solids* **58**, 1315 (1997).
- <sup>22</sup>B. S. Zou and V. Volkov, *J. Phys. Chem. Solids* **61**, 757 (2000).
- <sup>23</sup>G. F. Goya, T. S. Berquó, F. C. Fonseca, and M. P. Morales, *J. Appl. Phys.* **94**, 3520 (2003).
- <sup>24</sup>R. D. Zysler, D. Fiorani, A. M. Testa, L. Suber, E. Agostinelli, and M. Godinho, *Phys. Rev. B* **68**, 212408 (2003).
- <sup>25</sup>C. G. Shull, W. A. Strauser, and E. O. Wollan, *Phys. Rev.* **83**, 333 (1951).
- <sup>26</sup>R. H. Kodama, *J. Magn. Magn. Mater.* **200**, 359 (1999).
- <sup>27</sup>W. F. J. Fontijn, P. J. van der Zaag, L. F. Feiner, R. Metselaar, and M. A. C. Devillers, *J. Appl. Phys.* **85**, 5100 (1999).
- <sup>28</sup>W. F. J. Fontijn, P. J. van der Zaag, M. A. C. Devillers, V. A. M. Brabers, and R. Metselaar, *Phys. Rev. B* **56**, 5432 (1997).
- <sup>29</sup>Y. A. Barnakov, B. L. Scott, V. Golub, L. Kelly, V. Reddy, and K. L. Stokes, *J. Phys. Chem. Solids* **65**, 1005 (2004).